INORGANIC CHEMISTRY
FRONTIERS

RESEARCH ARTICLE

View Article Online
View Journal



Cite this: DOI: 10.1039/d6qi00419a

# Field-dependent $^{1}$H relaxometry as a general probe of hydration dynamics in paramagnetic $Ln^{3+}$ complexes

Marco Ricci, [a] Lorenzo Risolo, [a] Fabio Carniato, [a,b] Daniela Lalli, *[a,b] Carlos Platas-Iglesias [c] and Mauro Botta *[a,b]

Hydration dynamics at metal centres govern the reactivity of chemical and biological systems and are central to the function of paramagnetic probes. Nuclear magnetic resonance (NMR) offers powerful multinuclear and multifield approaches to interrogate exchange processes across broad kinetic regimes. However, established methodologies, such as variable temperature $^{17}$O NMR, require high sample concentrations, limiting access to poorly soluble, high-molecular-weight, or scarce complexes. Here we introduce a concentration-efficient relaxometric strategy that enables direct determination of water-exchange dynamics in paramagnetic complexes through the simultaneous analysis of longitudinal and transverse $^{1}$H relaxation rates over an extended magnetic field range. This approach provides quantitative access to exchange kinetics while requiring only dilute solutions. We validate the method using the [Ln(DTPA)]$^{2-}$ and [Ln(AAZTA)]$^{-}$ series, two prototypical systems in which lanthanide contraction modulates coordination number and hydration state in distinct ways. The DTPA complexes display the expected progressive acceleration of water exchange toward the heavier lanthanides, consistent with a dissociative interchange mechanism. In contrast, the AAZTA analogues exhibit a pronounced deceleration of exchange for the heavier ions, reflecting changes in coordination environment and hydration equilibria. The method faithfully captures these opposing trends, demonstrating its sensitivity to subtle structural variations across the series. Beyond reproducing established behaviour, this strategy expands experimental access to metal-water exchange kinetics under conditions previously inaccessible to conventional $^{17}$O NMR techniques. Its direct relevance to MRI contrast agent development enables rational optimization of next-generation probes for high-field imaging. More broadly, the methodology is readily extendable to transition-metal systems, offering a general platform to interrogate hydration dynamics in coordination chemistry.

Received 3rd March 2026,
Accepted 30th March 2026

DOI: 10.1039/d6qi00419a

rsc.li/frontiers-inorganic



## Introduction

The hydration of metal complexes is a fundamental reaction underlying several processes of chemical and biological relevance, including catalytic activity, ion transport, and drug efficacy.[1] The hydration process involves three key steps: (i) the formation of direct coordination bonds between the metal centre and the inner-sphere (IS) water molecule(s); (ii) hydrogen-bonding interactions between the first and second coordination spheres; and (iii) chemical exchange reactions between the hydration water molecules and the bulk. Of particular relevance is the exchange process involving the water molecules in the metal ion's inner coordination sphere, each characterized by an average residence lifetime, $\tau_M$.[1,2] This parameter can vary dramatically depending on the nature and oxidation state of the metal ion – for example, from a few hundred picoseconds in the $[Eu(H_2O)_7]^{2+}$ complex[3] to over 250 years for $[Ir(H_2O)_6]^{3+}$.[4] As a consequence, describing the water-exchange dynamics of the first and second hydration shells is essential for understanding a wide range of phenomena, including complex formation and substitution reactions, redox processes, metalloenzyme-catalysed transformations, metal-ion transport across cell membranes, and the performance of contrast agents (CAs) used in Magnetic Resonance Imaging (MRI). CAs are paramagnetic complexes that contain rapidly exchanging inner-sphere water molecules capable of shortening the longitudinal and transverse relaxation times ($T_1$ and $T_1$) of bulk water protons, thereby enhancing the intensity and contrast of their NMR signal.[5] CAs are generally classified into three main categories

[a]Dipartimento di Scienze e Innovazione Tecnologica Università del Piemonte Orientale, Viale T. Michel 11, Alessandria 15121, Italy.
E-mail: mauro.botta@uniupo.it, daniela.lalli@uniupo.it
[b]Magnetic Resonance Platform (PRISMA-UPO), Università del Piemonte Orientale, Alessandria, Italy
[c]Centro Interdisciplinar de Química e Bioloxía (CICA) and Departamento de Química, Facultade de Ciencias Universidade da Coruña, 15071 A Coruña, Galicia, Spain

based on their effects on $T_1$ and $T_2$: (i) positive CAs, which produce brighter images by increasing water-signal intensity through enhancement of the longitudinal relaxation rate ($R_1 = 1/T_1$); (ii) negative CAs, which yield darker images by reducing water-signal intensity as a result of shortened $T_2$; and (iii) paramagnetic chemical exchange saturation transfer (paraCEST) agents, which modulate signal intensity *via* exchange-mediated magnetization transfer.

Among the lanthanide ions, $Gd^{3+}$ is the most efficient relaxing agent, owing to its long electronic relaxation time associated with an isotropic distribution of unpaired electrons. Consequently, $Gd^{3+}$ complexes are widely used as positive CAs in clinical settings. Conversely, chelates of other lanthanide(III) ions with shorter electronic relaxation times have been explored as negative CAs, particularly for applications in modern high-field MRI scanners (>3 T). Beyond the electronic properties of the metal centre, the efficacy of CAs depends strongly on both the hydration number ($q$) and the water exchange rate ($k_{ex} = 1/\tau_M$). For $T_1$-shortening agents, optimal $\tau_M$ values for low-molecular-weight $Gd^{3+}$ complexes typically fall between 1 and 100 ns. In contrast, substantially longer $\tau_M$ values ($10^{-6}$–$10^{-3}$ s) are requested for CEST or $T_2$-based agents.[6–8] Given the pivotal role of $\tau_M$ in determining CA performance, accurately quantifying this parameter is essential for the rational design of optimized MRI probes. NMR spectroscopy provides a versatile toolkit for probing water-exchange dynamics, including line-shape analysis, relaxation-based methods, isotopic enrichment, and CEST techniques.[1] Water-exchange rates and their activation parameters are most commonly determined by measuring the temperature dependence of $R_2$ and the chemical shift of $^{17}$O-enriched water.[9,10] However, this approach requires high concentrations of $Gd^{3+}$ chelates (≈10–20 mM), and even one order of magnitude higher for other $Ln^{3+}$ ions.[11,12] While such conditions are feasible for small complexes with $\tau_M$ values spanning roughly 10–2000 ns,[13] they are often unattainable for macromolecular systems, whose limited solubility hampers the acquisition of reliable $^{17}$O NMR data.[14] Most notably, studies on water-exchange dynamics in $Ln^{3+}$ complexes other than $Gd^{3+}$ remain scarce;[15] the few available reports focus mainly on neutral or cationic chelates with slow $k_{ex}$ values and rely on diverse NMR methodologies.[11,12,16–20] Only recently combined $T_1$ and $T_2$ measurements have been applied to investigate three Ln(III)–DOTA complexes (Ln = Dy, Tb, Er) beyond $Gd^{3+}$, providing preliminary insights into water-exchange behaviour along the lanthanide series.[21] However, simultaneous data analysis has not been implemented, which may cause reduced fitting accuracy and even create bias. Moreover, systematic, series-wide studies are still lacking – despite their importance for identifying general trends in metal-hydration mechanisms.

In this work, we present a broadly applicable strategy for the systematic characterization of the hydration state and water-exchange dynamics of paramagnetic lanthanide chelates, enabling their analysis under dilute conditions. In practice, the detection limit is reached when the paramagnetic contribution to the solvent relaxation rate becomes comparable to the diamagnetic background of pure water (*ca.* 0.38 $s^{-1}$ at 298 K) or falls within the margin of instrumental error. The approach relies exclusively on proton NMR data and involves the simultaneous analysis of $T_1$ and $T_2$ relaxation times measured across a wide range of magnetic fields, corresponding to $^1$H Larmor frequencies from 30 to 600 MHz. We optimized and standardized the protocol using paramagnetic complexes that differ in net charge, hydration number, and rotational mobility. For each chelate, we examined how water-exchange dynamics evolve across the lanthanide series, from $Pr^{3+}$ to $Yb^{3+}$. In particular, we focused on two families of $Ln^{3+}$ complexes based on the DTPA and AAZTA ligands (Scheme 1), both of which have been extensively characterized using conventional techniques. These well-studied systems offer robust benchmarks for validating the reliability and general applicability of our method.

Beyond water-exchange dynamics, the proposed approach also provides access to key structural and magnetic parameters of paramagnetic Ln–chelates, enabling the identification of the distinct contributions to overall paramagnetic relaxation. By developing a comprehensive understanding of the main factors that govern inner-sphere water exchange in lanthanide complexes, we aim to facilitate the rational design of next-generation, high-efficiency MRI probes. As clinical MRI continues to move toward higher magnetic field strengths, the need for innovative contrast agents becomes increasingly pressing. In this context, $T_2$-specific $Ln^{3+}$ complexes and paraCEST probes show significant promise for future diagnostic applications.

## Results and discussion

The simultaneous analysis of the magnetic-field dependence of nuclear relaxation rates ($R_1$ and $R_2$), collected over a wide temperature range, is among the most direct and reliable approaches for characterizing water-exchange dynamics in paramagnetic complexes. Despite its advantages, this methodology is not yet widely adopted, largely because high-field relaxometers capable of providing a continuous range of magnetic fields are not routinely available. The recent introduction of a commercial high-field relaxometer capable of measuring relaxation rates up to 120 MHz now provides access to unprecedented high-field data. This development paves the way to obtaining rapid and reliable information on the hydration state and water-exchange dynamics of paramagnetic metal complexes, with levels of detail comparable to more estab-

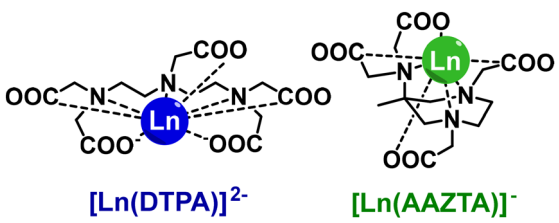


**Scheme 1** Chemical structures of $[Ln(DTPA)]^{2-}$ and $[Ln(AAZTA)]^{-}$.

lished techniques. To validate this approach, a systematic study of water-exchange behaviour was first conducted on well-defined model systems – namely, DTPA lanthanide complexes – whose hydration state and coordination geometry remain constant across the series. The methodology was then applied to the more structurally intricate $[Ln(AAZTA)]^-$ complexes, which undergo gradual structural changes along the lanthanide series resulting in reduced hydration. This second stage confirmed that the approach is sensitive to both changes in metal hydration and variations in water-exchange dynamics.

This methodology has been successfully applied to the study of all paramagnetic lanthanide ions, with the notable exception of $Gd^{3+}$, for which we utilized data derived from conventional characterization techniques. In the subsequent sections, we will first detail the equations employed to construct the theoretical model, followed by the presentation and discussion of the experimental results.

## Theoretical background

In metal-hydration reactions involving paramagnetic complexes, magnetic interactions between the water proton nuclei and the unpaired electrons of the metal centre lead to an increase in nuclear relaxation rates. This paramagnetic relaxation enhancement ($R_{i,p}$) is proportional to the concentration ($C$) of the paramagnetic species and to the relaxivity ($r_{1,2}$) (eqn (1)), defined as the increase in the relaxation rate of bulk water protons normalized to a 1 mM solution of the paramagnetic complex.[22]

$$R_{i,p} = r_{i,p} \times C \text{ with } i = 1, 2 \quad (1)$$

Three different contributions account for the relaxivity: (i) inner sphere (IS), (ii) second sphere (SS), and (iii) outer sphere (OS) (eqn (2)):[23]

$$r_i = r_i^{IS} + r_i^{SS} + r_i^{OS} \text{ with } i = 1, 2 \quad (2)$$

For hydrated complexes, the inner-sphere contribution typically dominates relaxivity and depends on both the hydration number ($q$) and the average residence lifetime ($\tau_M$) of the IS water molecules. Inner sphere longitudinal and transverse relaxivity are described by eqn (3) and (4):

$$r_1^{IS} = \frac{1}{1000} \times \frac{q}{55.55} \times \frac{1}{T_{1M} + \tau_M} \quad (3)$$

$$r_2^{IS} = \frac{1}{1000} \times \frac{q}{55.55} \times \frac{1}{\tau_M} \times \frac{{T_{2M}}^{-1}({T_{2M}}^{-1} + {\tau_M}^{-1}) + {\Delta\omega_M}^2}{({T_{2M}}^{-1} + {\tau_M}^{-1})^2 + {\Delta\omega_M}^2} \quad (4)$$

where $\Delta\omega_M$ is the proton chemical-shift difference between coordinated and bulk water, and $T_{1M}$ and $T_{2M}$ are the longitudinal and transverse relaxation times of the IS water molecules. $\Delta\omega_M$ can be estimated from the Larmor frequency difference ($\Delta\omega_p$) between bulk water protons in the presence and absence of the paramagnetic species of interest,[24] defined as:

$$\Delta\omega_p = fq \frac{\Delta\omega_M}{\left(1 + \frac{\tau_M}{T_{2M}}\right)^2 + {\tau_M}^2 {\Delta\omega_M}^2} \quad (5)$$

where $f$ represents the ratio between the concentration of the paramagnetic species and that of bulk water. In the fast-exchange regime ${\tau_m}^2{\Delta\omega_M}^2 \ll 1$ and $\tau_M/T_{2M} \ll 1$, thus eqn (5) can be simplified to:

$$\Delta\omega_p = fq\Delta\omega_M \quad (6)$$

In the case of $Ln^{3+}$ chelates, these conditions are usually met by complexes exhibiting a relatively fast water exchange rate ($k_{ex} = 1/\tau_M \sim 10^7$–$10^9$ $s^{-1}$). $T_{1M}$ and $T_{2M}$ are defined as the sum of the dipole–dipole (DD), scalar (SC) and Curie (Cu) mechanisms:[23]

$$\frac{1}{T_{iM}} = \frac{1}{T_i^{DD}} + \frac{1}{T_i^{SC}} + \frac{1}{T_i^{Cu}} \text{ with } i = 1, 2 \quad (7)$$

Their contribution to $T_{iM}$ is described by the Solomon–Bloembergen–Morgan (SBM) equations,[25–28] reported in the SI (eqn (S7)–(S10)). For clarity, only the dipole–dipole terms are shown here:

$$\left(\frac{1}{T_1^{DD}}\right)^{IS} = \frac{2}{15}\left(\frac{\mu_0}{4\pi}\right)^2 \frac{{\gamma_I}^2 {g_J}^2 {\mu_B}^2}{r^6} J(J+1)\left[\frac{7\tau_{c2}}{1 + {\omega_S}^2{\tau_{c2}}^2} + \frac{3\tau_{c1}}{1 + {\omega_I}^2{\tau_{c1}}^2}\right] \quad (8)$$

$$\left(\frac{1}{T_2^{DD}}\right)^{IS} = \frac{1}{15}\left(\frac{\mu_0}{4\pi}\right)^2 \frac{{\gamma_I}^2 {g_J}^2 {\mu_B}^2}{r^6} J(J+1) \left[\frac{13\tau_{c2}}{1 + {\omega_S}^2{\tau_{c2}}^2} + \frac{3\tau_{c1}}{1 + {\omega_I}^2{\tau_{c1}}^2} + 4\tau_{c1}\right] \quad (9)$$

where $\mu_0$ is the vacuum magnetic permeability; $\gamma_I$ is the nuclear gyromagnetic ratio; $g_J$ is the Landé $g$-factor; $\mu_B$ is the Bohr magneton; $r$ is the nuclear spin-electron distance; $J$ is the total spin quantum number,[29] whose values are reported in Table S1; $\tau_c$ is the correlation time modulating the dipolar interaction; and $\omega_I$ and $\omega_S$ are the nuclear and electron Larmor frequencies, which depend on the magnetic field strength. The magnetic field dependence of longitudinal and transverse relaxivity is determined through $^1H$ Nuclear Magnetic Relaxation Dispersion (NMRD) profiles. Because $r_1^{IS}$ and $r_2^{IS}$ depend strongly on the number of metal-bound water molecules and on their residence lifetime, respectively (Fig. 1), the simultaneous analysis of $1/T_1$ and $1/T_2$ $^1H$ NMRD profiles enables a direct determination of both the hydration state and the water exchange dynamics. These parameters are among the most critical to optimize when aiming to design more efficient MRI contrast agents.

## The $[Ln(DTPA)(H_2O)]^{2-}$ series

Still widely used in diagnostic imaging, $[Gd(DTPA)(H_2O)]^{2-}$ was the first contrast agent approved for clinical settings. Its structure and water-exchange properties have been thoroughly characterized using conventional techniques.[30–35] The DTPA ligand acts as an octadentate chelator, fully utilizing its binding sites to form thermodynamically stable complexes with lanthanide(III) ions. These complexes adopt a tricapped trigonal prismatic geometry, where a single coordinated water molecule occupies one of the three capping positions. In solu-

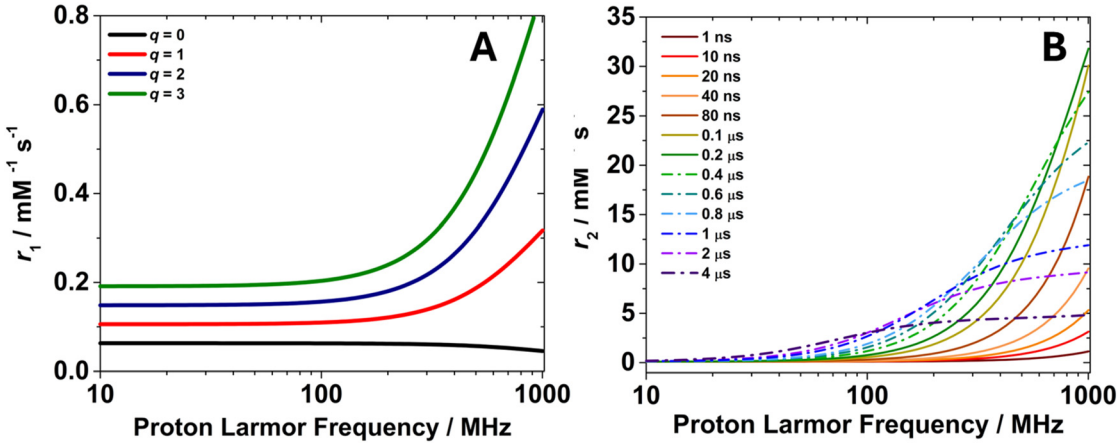


**Fig. 1** Proton longitudinal and transverse relaxivity as a function of the proton Larmor frequency. The $r_1$ dependence on the hydration number ($q$) was calculated for a $Dy^{3+}$ complex with $\tau_M$ = 27 ns, $\tau_S$ = 0.2 ps, $\tau_R$ = 70 ps, $r_{LnH}$ = 3.0 Å, $T$ = 298 K, (A). The $r_2$ dependence on the residence lifetime ($\tau_M$) was calculated for a $Dy^{3+}$ complex with $q$ = 1, $\tau_S$ = 0.2 ps, $\tau_R$ = 70 ps, $r_{LnH}$ = 3.0 Å, $\Delta\omega_M$ = 1.4 × $10^5$ rad $s^{-1}$ $T^{-1}$, $T$ = 298 K (B).

tion, these complexes are stereochemically non-rigid. They exhibit fluxional behavior driven by two simultaneous processes: the conformational inversion of the ethylenediamine backbone and the rotation of the acetate arms. Together, these movements result in the continuous interconversion between two enantiomeric forms.[35] Isostructurality across the lanthanide series has been inferred from NMR studies and conclusively confirmed by crystallographic analyses spanning the Nd–Yb range.[36–40] Notably, the $[Ln(DTPA)(H_2O)]^{2-}$ complexes remain free of isomeric species in solution throughout the series.[35] These features make the $[Ln(DTPA)(H_2O)]^{2-}$ complexes an excellent model system for probing how water-exchange dynamics depend on the lanthanide ionic radius. To date, $k_{ex}$ values have been reported only for the $Gd^{3+}$ ($k_{ex}$ = 3.3 × $10^6$ $s^{-1}$) and $Dy^{3+}$ ($k_{ex}$ = 34.5 × $10^6$ $s^{-1}$) DTPA complexes.[15,34] Our first objective is therefore to validate the proposed methodology by comparing our results with these established data. Subsequently, by completing the relaxometric characterization of the entire $[Ln(DTPA)(H_2O)]^{2-}$ series, we aim to elucidate the key factors governing the dependence of $k_{ex}$ on the lanthanide contraction in $q$ = 1 chelates.

Initial analyses were intentionally conducted at $[Ln(DTPA)]^{2-}$ concentrations of approximately 25 mM (Table S2) to establish a robust dataset required to rigorously assess the effectiveness of the proposed methodology. The $1/T_1$ and $1/T_2$ $^1$H NMRD profiles were recorded for the $[Ln(DTPA)]^{2-}$ chelates at 298 K over a proton Larmor frequency range of 30–600 MHz (Fig. 2). All complexes display low longitudinal relaxivity values ($r_1$ < 0.5 $mM^{-1}$ $s^{-1}$), consistent with their short electronic relaxation times, which severely limit the efficiency of paramagnetic relaxation enhancement (Fig. 2A). For $Yb^{3+}$ and for the light lanthanides ($Nd^{3+}$, $Pr^{3+}$), $r_1$ remains essentially zero across the entire magnetic-field range. In contrast, the heavier lanthanides ($Tb^{3+}$, $Dy^{3+}$, $Ho^{3+}$, and $Er^{3+}$) show a modest increase in $r_1$ at high frequencies (>300 MHz), attributable to the Curie contribution to nuclear relaxation, which scales with the square of the magnetic field and the fourth power of the magnetic moment (eqn (S18)).[41]

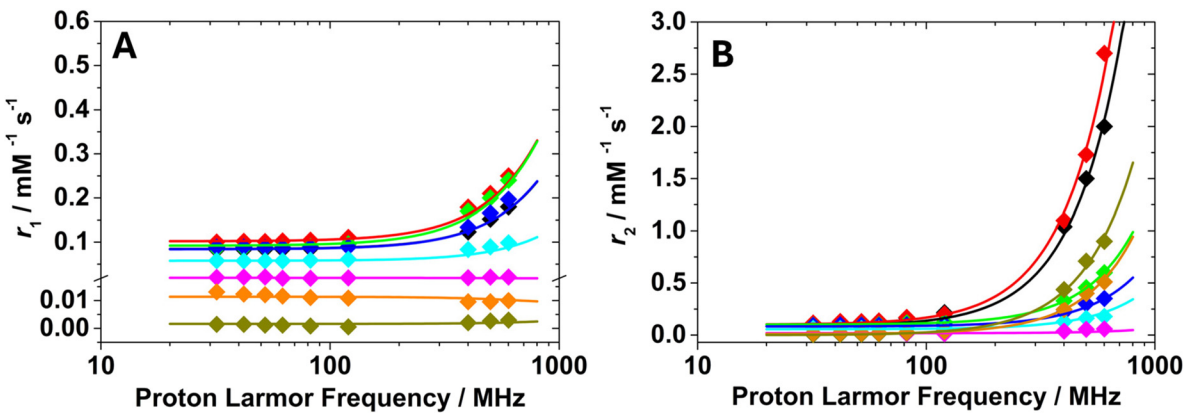


**Fig. 2** $1/T_1$ (A) and $1/T_2$ (B) $^1$H NMRD profiles recorded for $[Ln(DTPA)]^{2-}$ complexes (♦ = Pr, ♦ = Nd, ♦ = Tb, ♦ = Dy, ♦ = Ho, ♦ = Er, ♦ = Tm, ♦ = Yb) at pH 7.0 and 298 K.

As a result, the field dependence of longitudinal relaxation is more pronounced for lanthanide ions with larger magnetic moments ($Tb^{3+}$–$Tm^{3+}$), as shown in Fig. 2A and previously reported for the lanthanide aqua ions,[42] which is mainly due to the Curie contribution to relaxation (Fig. 3A). In contrast, the $r_2$ NMRD profiles display a low-field plateau between 30 and 120 MHz, followed by a pronounced increase in relaxivity at higher frequencies (>120 MHz), the magnitude of which depends on the specific lanthanide ion (Fig. 2B). The presence of a plateau indicates that, within this field range, the correlation time governing the electron–nucleus dipolar interaction is dominated by the electronic term, which is effectively field-independent. At higher frequencies, the observed rise in relaxivity is driven primarily by the increase in $\Delta\omega_M$ and, to a lesser extent, by Curie relaxation, as shown in Fig. 3B and previously reported.[43–45]

The experimental data were analysed through a global fitting procedure of the longitudinal and transverse $^1$H NMRD profiles. The fit showed strong agreement with the experimental observations, and the resulting set of parameters is summarized in Table 1.

To support the fitting procedure, several structural and dynamic parameters influencing the $r_1$ and $r_2$ data were fixed to the values established for the $[Gd(DTPA)]^{2-}$ complex: the number of inner-sphere water molecules ($q$ = 1), the rotational correlation time ($\tau_R$ = 70–72 ps), and the distance between the protons of outer-sphere water molecules and the $Ln^{3+}$ ion ($a_{Ln-H}$ = 4.0 Å). Additional parameters were determined independently. Specifically, $\Delta\omega_M$ values were estimated for each complex by measuring the chemical shift difference between Ln-bound and bulk water (Fig. S1 and Table 1), while inner-sphere Ln–$H_w$ distances ($r$) were obtained through DFT geometry optimizations, which were performed at the wB97XD/Def2-TZVPP[47,48] level using the large-core approximation[49] (see computational details). In these calculations, both implicit[50] and explicit solvation models were considered, incorporating a few explicit second-sphere water molecules to provide more realistic Ln–$H_w$ distances[51,52] (Fig. 4). The experimental $\Delta\omega_M$ values provide a good linear correlation with Bleaney's constants (Fig. S2), indicating that the $^1$H paramagnetic shifts are largely pseudocontact in origin and the complexes remain isostructural across the lanthanide series.[53]

With these constraints, the fitting procedure reduces to only two free parameters, $\tau_s$ and $\tau_M$, thereby minimizing covariance and yielding more robust and accurate results. To further validate the approach, the fitting residuals were analysed (see SI, Fig. S3). The residuals are symmetrically distributed around zero across the entire dataset, with no evidence of systematic deviation. Slightly larger – yet still minimal – residuals are observed at higher magnetic field strengths (400–600 MHz), consistent with the field dependence of $r_1$ and

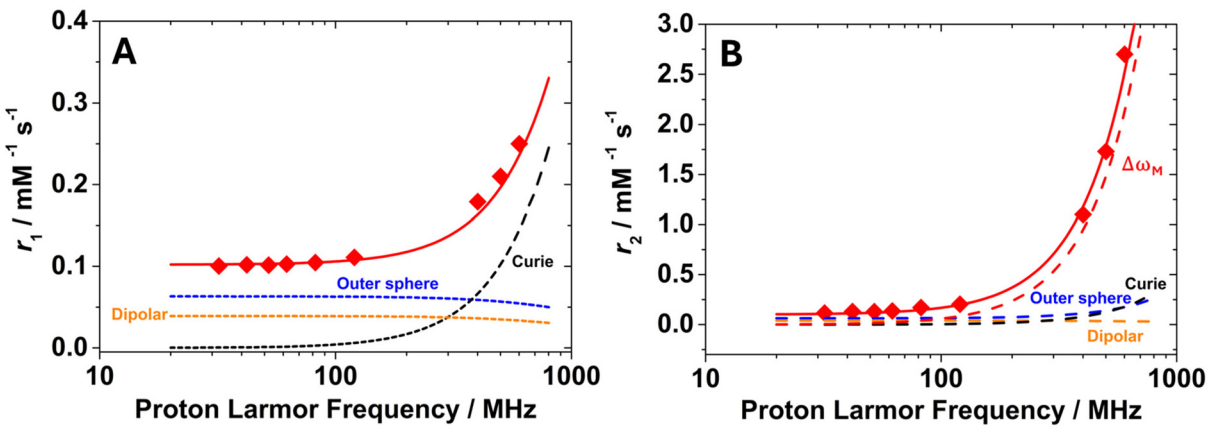


**Fig. 3** $1/T_1$ (A) and $1/T_2$ (B) $^1$H NMRD profiles recorded for the $[Dy(DTPA)]^{2-}$ complex at pH 7.0 and 298 K. The red solid line represents the best fit of the experimental data, while the dashed lines indicate the individual contributions: inner-sphere Curie (black), inner-sphere dipolar (orange), outer-sphere (blue), and chemical-shift (red).

**Table 1** Parameters obtained from the simultaneous analysis of $1/T_1$ and $1/T_2$ NMRD profiles at 298 K for $[Ln(DTPA)]^{2-}$

| Parameters | $Pr^{3+}$ | $Nd^{3+}$ | $Tb^{3+}$ | $Dy^{3+}$ | $Ho^{3+}$ | $Er^{3+}$ | $Tm^{3+}$ | $Yb^{3+}$ |
|---|---|---|---|---|---|---|---|---|
| $^{298}\tau_S$/ps | 0.03 ± 0.01 | 0.21 ± 0.01 | 0.20 ± 0.01 | 0.20 ± 0.01/0.14$^b$ | 0.18 ± 0.01 | 0.20 ± 0.01 | 0.22 ± 0.01 | 0.20 ± 0.01 |
| $^{298}\tau_R$/ps | 70$^a$ | 70$^a$ | 71$^a$ | 71$^a$/85$^b$ | 72$^a$ | 72$^a$ | 72$^a$ | 72$^a$ |
| $^{298}\tau_M$/ns | 340 ± 7 | 295 ± 6 | 28.4 ± 0.6 | 27.8 ± 0.7/29.0$^b$ | 12.2 ± 0.4 | 8.0 ± 1.0 | 4.1 ± 1.1 | 2.5 ± 1.4 |
| $q$ | 1$^a$ | 1$^a$ | 1$^a$ | 1$^a$/1$^b$ | 1$^a$ | 1$^a$ | 1$^a$ | 1$^a$ |
| $r$/Å | 3.17$^a$ | 3.16$^a$ | 3.09$^a$ | 3.08$^a$/3.1$^b$ | 3.07$^a$ | 3.06$^a$ | 3.05$^a$ | 3.04$^a$ |
| $a$/Å | 4.0$^a$ | 4.0$^a$ | 4.0$^a$ | 4.0$^a$ | 4.0$^a$ | 4.0$^a$ | 4.0$^a$ | 4.0$^a$ |
| $\Delta\omega_M/10^5$ rad s$^{-1}$ T$^{-1}$ | −0.3$^a$ | −0.2$^a$ | −1.3$^a$ | −1.5$^a$/−1.5$^b$ | −0.7$^a$ | 0.5$^a$ | 0.8$^a$ | 0.3$^a$ |

$^a$ Fixed during the fitting. $^b$ Parameters from literature.[46]

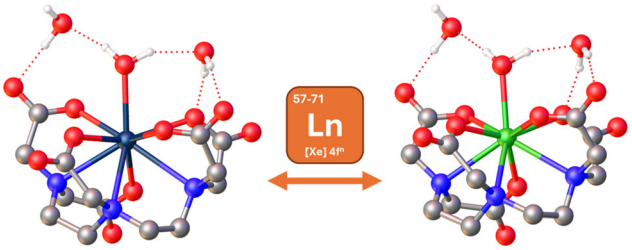


**Fig. 4** Schematic representation of the DFT optimized geometries of the $La^{3+}$ and $Lu^{3+}$ complexes of DTPA. $[Ln(DTPA)]^{2-}$ complexes are essentially isostructural across the lanthanide series.

$r_2$. Because the largest variations in relaxation rates occur in this high-field regime, the model is expected to exhibit greater absolute deviations in this region. Overall, the random distribution of the residuals supports the validity of the theoretical model and confirms the reliable extraction of hydration parameters without underlying systematic bias. Furthermore, the residual sum of squares (RSS), evaluated as a function of $\tau_M$ and $\tau_S$, defines a surface with a well-resolved global minimum, underscoring the robustness of the fitting procedure (Fig. S4). The resulting $\tau_s$ values fall within the expected range for $Ln^{3+}$ complexes ($\tau_s \approx 10^{-13}$ s),[54–56] reflecting the anisotropic electronic distribution of the 4f orbitals. Notably, $\tau_M$ exhibits a clear and systematic trend across the lanthanide series, as shown by the plot of $k_{ex}$ *versus* ionic radius[57] (Fig. 5). The light lanthanides ($Pr^{3+}$ and $Nd^{3+}$) exhibit $\tau_M$ values comparable to $[Gd(DTPA)]^{2-}$, for which $\tau_M$ values around 300 ns were reported.[32,34,40] Conversely, heavier lanthanides display progressively faster water exchange rates along the series, with the shortest residence time observed for $[Yb(DTPA)]^{2-}$ ($\tau_M$ = 2.5 ns). This behaviour can be attributed to the lanthanide contraction: as the ionic radius decreases, steric hindrance around the metal centre increases, rendering the coordinated water molecule more labile and reducing its residence time. This

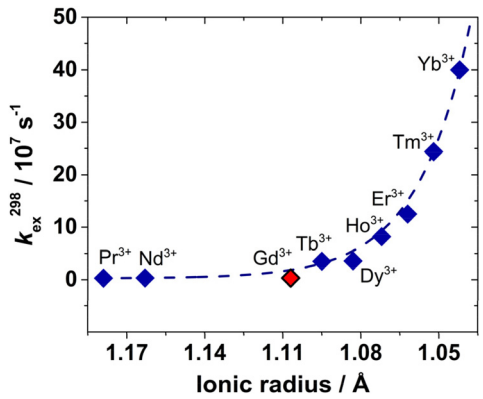


**Fig. 5** Plot of the $k_{ex}^{298}$ values calculated for the $[Ln(DTPA)]^{2-}$ complexes as a function of the $Ln^{3+}$ ionic radius for coordination number 9. For $[Gd(DTPA)]^{2-}$, the average of the values reported in the literature (303 ns)[32,34,40] was considered.

hypothesis is supported by DFT analyses, which provide insights into the Ln–$O_w$ distances and bond strengths. The latter were quantified by calculating the electron densities at the corresponding bond critical points ($\rho_{BCP}$) (Fig. S5). Notably, Ln–$O_w$ distances derived from X-ray structures show significant variability, differing by up to 0.2 Å even for the same complex (Fig. S6). This highlights their strong dependence on crystal packing effects and limits their reliability for establishing structure–dynamics correlations. For this reason, we turned to DFT calculations.

Interestingly, the Ln–$O_w$ distance decreases along the series as a result of the reduction in ionic radius, but simultaneously $\rho_{BCP}$ decreases, indicating a weakening of the Ln–$O_w$ bonds. Previous studies have shown that in lanthanide(III) complexes, the interaction with a ligand at a sterically demanding capping position can weaken as it shortens across the series,[58,59] in apparent violation of Badger's rule.[60] Accordingly, the lower $\rho_{BCP}$ values observed for the heavier lanthanide ions correspond to more labile Ln–$O_w$ bonds, indicative of faster water exchange rates. Consistent with this interpretation, a plot of the calculated Ln–$O_w$ distance (derived from DFT calculations; see SI) *versus* $k_{ex}$ (Fig. S7) reveals a trend closely mirroring that shown in Fig. 5. A similar trend has been reported for the DTPA bis methylamide derivative series [Ln(DTPA-BMA)], suggesting a comparable water exchange dissociative mechanism.[2] Given the structural homology between the ligands, it is reasonable to assume that the observed behaviour stems from similar factors: in the [Ln(DTPA-BMA)] series, the lanthanide contraction leads to increased steric congestion within the first coordination sphere, which in turn weakens the Ln–$O_w$ interaction. These structural changes have a pronounced impact on both the mechanism and the rate of water exchange, where the enhanced steric crowding results in a marked acceleration from $Gd^{3+}$ to $Ho^{3+}$, reflecting a mechanistic shift from an interchange-activated pathway to a predominantly dissociative process. This interpretation is supported by the systematic increase in activation entropy observed along the series, consistent with a growing dissociative character of the exchange reaction.[2]

### The AAZTA series

AAZTA (6-amino-6-methylperhydro-1,4-diazepinetetraacetic acid) is a mesocyclic chelating agent that forms thermodynamically stable complexes with lanthanide(III) ions. In the solid state, the $[Gd(AAZTA)]^-$ complex adopts a dimeric structure in which each $Gd^{3+}$ ion is ten-coordinate and displays a bicapped square-antiprismatic geometry. Within each AAZTA ligand, three of the four carboxylate groups bind to a single $Gd^{3+}$ center in a monodentate fashion, whereas the fourth carboxylate acts as a bridging group between two centrosymmetrically related $Gd^{3+}$ ions, sharing one oxygen atom between the two metal centers. The coordination sphere of each $Gd^{3+}$ ion is further completed by the three nitrogen donors of the diazepine ring and by one inner-sphere water molecule.[61] In aqueous solution, $[Gd(AAZTA)]^-$ is nine-coordinate and features two inner-sphere water molecules. The exchange rate of

these coordinated water molecules was accurately determined by variable-temperature $^{17}O$ NMR measurements, specifically through analysis of the transverse relaxation rate ($R_2$) and the paramagnetic chemical shift ($\Delta\omega$). From these data, an effective water-exchange rate constant of $1.1 \times 10^7$ $s^{-1}$ was obtained at 298 K under neutral pH conditions.[62] In marked contrast, $[Yb(AAZTA)]^-$ contains only a single inner-sphere water molecule, whose residence lifetime is exceptionally long.[63] Indeed, the exchange is sufficiently slow so that the resonance of the coordinated water molecule could be directly observed in the $^1H$ NMR spectrum of the aqueous solution near room temperature. This observation represents the first reported example of an NMR signal ($\delta$ = 83 ppm) arising from a water molecule bound to a paramagnetic ion in an anionic complex. The unusually slow exchange dynamics enabled an efficient magnetization transfer experiment: selective saturation of the resonance at 83 ppm clearly revealed the presence of a pool of slowly exchanging protons. On the basis of these experiments, the residence lifetime of the coordinated water molecule in $[Yb(AAZTA)]^-$ was estimated to be approximately 150 μs at 293 K, *i.e.*, about four orders of magnitude longer than that measured for the $[Gd(AAZTA)]^-$ analogue.[64] High-resolution $^1H$ NMR spectroscopy, DFT calculations, and X-ray diffraction data consistently point to the occurrence of a structural transition along the lanthanide series, located between $Ho^{3+}$ and $Er^{3+}$ and associated with a reduction of the hydration number from $q$ = 2 to $q$ = 1.[16] DFT calculations indicate that the $[Ln(AAZTA)]^-$ complexes can adopt two distinct and energetically stable coordination geometries, namely a monocapped square antiprism ($q$ = 2) and a dodecahedron ($q$ = 1). The bishydrated monocapped square-antiprismatic geometry is energetically favored for the larger lanthanide ions ($La^{3+}$–$Ho^{3+}$), whereas the monohydrated dodecahedral structure becomes more stable for the smaller ions ($Er^{3+}$–$Lu^{3+}$). DFT analysis further provides insight into the evolution of metal–water interactions along the series. In particular, the contraction of the lanthanide ionic radius leads to a progressive shortening of the Ln–$O_w$ distance for one inner-sphere water molecule. In contrast, the Ln–$O_w$ distance associated with the second coordinated water increases for the heavier lanthanides, reflecting enhanced steric crowding within the first coordination sphere. These structural changes are directly mirrored in the water-exchange dynamics of the $[Ln(AAZTA)]^-$ complexes. Notably, the transition from bishydrated to monohydrated species is accompanied by a dramatic slowdown of the exchange process, spanning nearly three orders of magnitude. For the bishydrated $[Gd(AAZTA)(H_2O)_2]^-$ complex, two distinct residence lifetimes were measured for the inner-sphere water molecules ($\tau_{MA}$ = 29 ns and $\tau_{MB}$ = 169 ns), consistent with inequivalent coordination environments.[64] This peculiar behaviour was also observed in the case of $Gd^{3+}$ complexes of AAZTA derivatives conjugated to amino acids.[65] In contrast, the monohydrated $[Yb(AAZTA)(H_2O)]^-$ complex exhibits an exceptionally long residence lifetime ($\tau_M$ = 157 μs), highlighting the profound impact of hydration state and coordination geometry on water-exchange kinetics.[63] In this context, evaluating whether the proposed methodology can capture such pronounced variations in hydration number and exchange dynamics across the $Ln^{3+}$ series, even in a structurally complex system such as $[Ln(AAZTA)]^-$, represents a particularly stringent and informative test. This second series of analyses was conducted using more dilute solutions of $[Ln(AAZTA)]^-$ to evaluate the sensitivity of the method. $Pr^{3+}$ (7 mM) and $Nd^{3+}$ (9 mM) were intentionally selected as representative cases due to their low inherent relaxivity (Table S2), thereby establishing the practical performance limits of the strategy. The $1/T_1$ and $1/T_2$ $^1H$ NMRD curves were collected on the $[Ln(AAZTA)]^-$ chelates at 298 K over the $^1H$ Larmor frequency range 30 to 600 MHz (Fig. 6).

The longitudinal and transverse NMRD profiles closely resemble those measured for the $[Ln(DTPA)]^{2-}$ series, with the notable exception of the $1/T_2$ profiles of $[Dy(AAZTA)]^-$ and $[Ho(AAZTA)]^-$. In these two cases, a pronounced increase in $r_2$ is observed at high magnetic fields (>50 MHz), followed by the emergence of a plateau at higher fields, where the condition $\Delta\omega_M \times \tau_M \approx 1$ is fulfilled, in agreement with predictions from paramagnetic relaxation theory.[41] Simultaneous fitting of the longitudinal and transverse NMRD profiles yields an excellent

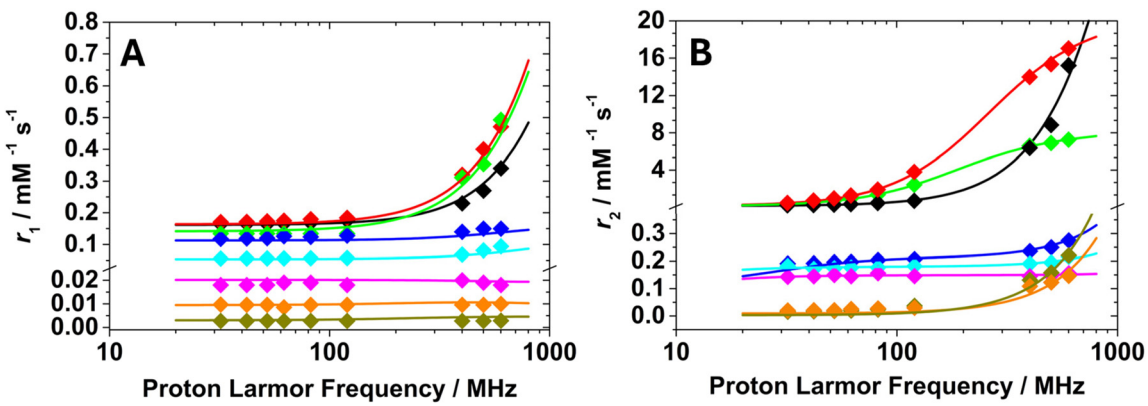


**Fig. 6** $1/T_1$ (A) and $1/T_2$ (B) $^1H$ NMRD profiles recorded for $[Ln(AAZTA)]^-$ complexes (◆ = Pr, ◆ = Nd, ◆ = Tb, ◆ = Dy, ◆ = Ho, ◆ = Er, ◆ = Tm, ◆ = Yb) at pH 7.0 and 298 K.

agreement with the experimental data and allows reliable extraction of the parameters reported in Table 2. To reduce the number of adjustable variables and limit parameter covariance, several quantities were fixed to established values, including the rotational correlation time ($\tau_R$ = 74–76 ps) and the distance between outer-sphere water molecules and the lanthanide ion ($a_{Ln-H}$ = 4.0 Å). The average distances of the coordinated water molecules from the metal centre were instead obtained from DFT geometry optimizations (Fig. 7 and see SI).

In contrast to the $[Ln(DTPA)]^-$ complexes, the $\Delta\omega_M$ values for the $[Ln(AAZTA)]^{2-}$ chelates were treated as fitting parameters. This approach was necessary because the longer water residence lifetimes characteristic of the AAZTA complexes result in small $\Delta\omega_p$ values, which are difficult to determine experimentally with sufficient accuracy. The fits of the data afford absolute values of $\Delta\omega_M$, as this parameter appears as a square term in eqn (4).

The hydration number along the lanthanide series was estimated by comparing the low-field $r_1$ values of the $[Ln(AAZTA)]^-$ complexes with those of the corresponding $[Ln(DTPA)]^{2-}$ chelates (Fig. S8). The $[Ln(AAZTA)]^-$ series exhibits an approximately twofold increase in $r_1$ from $Pr^{3+}$ to $Ho^{3+}$, consistent with the presence of two inner-sphere water molecules, while comparable $r_1$ values are observed for $Tm^{3+}$ and $Yb^{3+}$, indicative of monohydrated species. At low magnetic fields, $r_1$ is directly proportional to the hydration number $q$, as illustrated by the simulations reported in Fig. 1A. Notably, the $r_1$ value measured for $[Er(AAZTA)]^-$ is approximately 30% higher than that of $[Er(DTPA)]^{2-}$, likely reflecting the presence of a minor population of the bis-hydrated complex in solution. Indeed, literature DFT studies on mono- and bis-hydrated $[Ln(AAZTA)]^-$ structures show that, along the lanthanide series, the monohydrated structure becomes progressively more stabilized for heavier ions.[16] However, $Er^{3+}$ lies at the point along the lanthanide series where the energetic difference between the mono- and bis-hydrated forms is smaller, making the coexistence of a minor bis-hydrated population plausible despite the predominance of the monohydrated species, as also supported by single-crystal X-ray diffraction data,[16] and sufficient to account for the slightly increased $r_1$ value observed. Based on these observations, the corresponding $q$ values were fixed during the fitting of the experimental NMRD data. The fitting procedure showed excellent agreement with the experimental profiles. Consistent with the DTPA series, an analysis of the fitting residuals for these complexes provided analogous results, further confirming the absence of systematic deviations and the overall robustness of the model (see SI, Fig. S9). The resulting parameters are summarized in Table 2. As observed for the $[Ln(DTPA)]^{2-}$ complexes, the $\tau_S$ values fall in the range 0.04–0.28 ps, in agree-

**Table 2** Parameters obtained from the simultaneous analysis of the $1/T_1$ and $1/T_2$ NMRD profiles at 298 K for the $[Ln(AAZTA)]^-$ chelates

| Parameters | $Pr^{3+}$ | $Nd^{3+}$ | $Tb^{3+}$ | $Dy^{3+}$ | $Ho^{3+}$ | $Er^{3+}$ | $Tm^{3+}$ | $Yb^{3+}$ |
|---|---|---|---|---|---|---|---|---|
| $^{298}\tau_S$/ps | 0.04 ± 0.01 | 0.12 ± 0.01 | 0.27 ± 0.01 | 0.22 ± 0.01 | 0.19 ± 0.01 | 0.28 ± 0.01 | 0.20 ± 0.01 | 0.20 ± 0.01 |
| $^{298}\tau_R$/ps | 74[a] | 74[a] | 74[a] | 75[a] | 75[a] | 76[a] | 76[a] | 76[a] |
| $^{298}\tau_M$ | 63 ± 5 ns | 60 ± 6 ns | 296 ± 13 ns | 1.8 ± 0.1 μs | 4.6 ± 0.1 μs/ 172 ± 88 μs[c] −12 ± 1 μs[c] | 126 ± 3 μs/ 11 ± 1 μs[c] | 121 ± 1 μs/ 14 ± 1 μs[c] | 131 ± 1 μs/ 157 ± 17 μs[d], 149 ± 12 μs[e] |
| $q$ | 2[a] | 2[a] | 2[a] | 2[a] | 2[a] | 1[a] | 1[a] | 1[a] |
| $r$/Å | 3.12[a] | 3.11[a] | 3.06[a] | 3.03[a] | 3.02[a] | 2.95[a] | 2.94[a] | 2.94[a] |
| $a$/Å | 4.0[a] | 4.0[a] | 4.0[a] | 4.0[a] | 4.0[a] | 4.0[a] | 4.0[a] | 4.0[a] |
| $\Delta\omega_M/10^5$ rad $s^{-1}$ $T^{-1}$ [b] | 0.21 ± 0.01 | 0.17 ± 0.01 | 0.85 ± 0.1 | 0.91 ± 0.1 | 0.50 ± 0.1 | 0.21 ± 0.1 | 0.68 ± 0.1 | 0.50 ± 0.1 |

[a] Fixed during the fitting. [b] The fits of the data yield absolute values. [c] CEST data (278 K; ref. 16). For $Ho^{3+}$, the $\tau_M$ values of both water molecules are reported. [d] $^1$H NMR lineshape analysis (293 K, ref. 63). [e] CEST data (293 K; ref. 63).

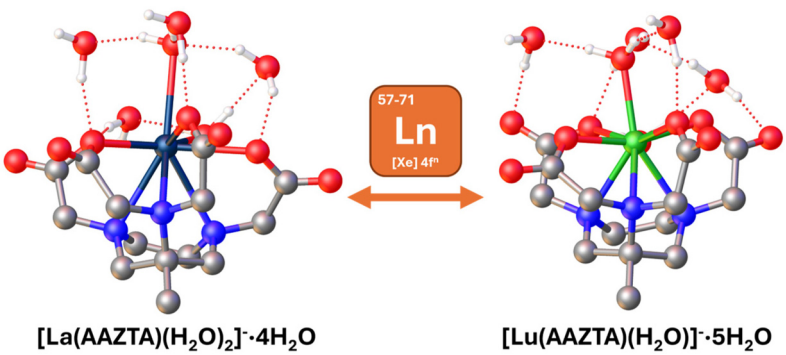


**Fig. 7** Schematic representation of the DFT optimized geometries of the $La^{3+}$ and $Lu^{3+}$ complexes of AAZTA. $[Ln(AAZTA)]^-$ experience a change in the number of coordinated water molecules from $q$ = 2 to $q$ = 1 (between $Ho^{3+}$ and $Er^{3+}$) across the lanthanide series.

ment with those typically reported for $Ln^{3+}$ chelates.[42,54–56] More importantly, reliable estimates of both $\Delta\omega_M$ and $\tau_M$ were obtained across the lanthanide series. The resulting $\Delta\omega_M$ values are in good agreement with literature data. Notably, the water-exchange rates exhibit a trend along the series that is opposite to that observed for the $[Ln(DTPA)]^{2-}$ complexes. The dependence of $k_{ex}$ on the ionic radius reveals relatively fast water-exchange dynamics for the light lanthanides, with $\tau_M \approx$ 60 ns for $Pr^{3+}$ and $Nd^{3+}$. Along the series, the exchange rate progressively decreases, slowing by nearly four orders of magnitude and reaching $\tau_M \approx 130$ μs for $Er^{3+}$, $Tm^{3+}$ and $Yb^{3+}$ (Fig. 8). A comparable trend is observed when substituting the ionic radius with the calculated Ln–$O_w$ distance (from DFT optimizations, Fig. S10), reflecting the parallel decrease of both parameters across the series.

The $\tau_M$ value determined here for $[Yb(AAZTA)]^-$ is in excellent agreement with previously reported $^1$H lineshape analysis and CEST measurements at 293 K, further supporting the robustness and reliability of the present approach for probing water-exchange dynamics across the lanthanide series (Table 2). For the complexes involving the other ions ($Ho^{3+}$, $Er^{3+}$, and $Tm^{3+}$), the agreement is less satisfactory, even when accounting for the temperature difference (278 *vs.* 298 K). In these cases, the slow exchange condition is not strictly satisfied; consequently, the values estimated from the CEST data are only rough approximations, likely subject to substantial uncertainty.[16] This pronounced trend can be attributed to the increasing steric compression associated with lanthanide contraction, which strengthens the interaction with the more tightly bound inner-sphere water molecule, leading to long residence lifetimes ($\tau_M \approx 130$ μs), while simultaneously favouring the dissociation of the more labile water molecule in complexes such as $[Er(AAZTA)]^-$. A comparable behaviour has been reported for AAZTAPh-$NO_2$ complexes of $Gd^{3+}$, $Dy^{3+}$, and $Tm^{3+}$,[12] supporting the generality of this mechanistic interpretation.

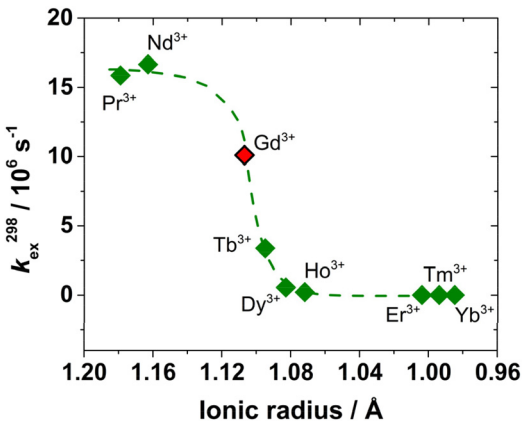


**Fig. 8** Plot of the water-exchange rates ($^{298}k_{ex}$) measured for the [Ln(AAZTA)]$^-$ complexes as a function of the lanthanide ionic radius. For [Gd(AAZTA)]$^-$, the average water residence lifetime of the two inner sphere water molecules (99 ns) was considered.[64]

### $1/T_1$ and $1/T_2$ $^1$H NMRD profiles as a function of temperature

Because the correlation times governing relaxivity are inherently temperature dependent, analysing relaxivity as a function of both temperature and magnetic field greatly enriches the experimental dataset and enables a more comprehensive description of the system.[9] The simultaneous fitting of these data within an appropriate theoretical framework provides robust estimates of the underlying molecular parameters and reduces ambiguities arising from parameter covariance. Moreover, the observed temperature dependence of molecular parameters like $\tau_R$ and $\tau_S$ is consistent with an Arrhenius-type behaviour (eqn (10)), offering additional insight into the energetic landscape that controls molecular motion and water-exchange dynamics:

$$\tau = \tau^{298} \exp\left\{\frac{-E_a}{R}\left(\frac{1}{298.15} - \frac{1}{T}\right)\right\} \quad (10)$$

On the other hand, $k_{ex}$ follows an Eyring behaviour:[66]

$$k_{ex} = \frac{1}{\tau_M} = k_{ex}^{298} \cdot \frac{T}{298.15}\exp\left\{\frac{\Delta H_M}{R}\left(\frac{1}{298.15} - \frac{1}{T}\right)\right\} = \frac{k_B T}{h}\exp\left(\frac{\Delta S^{\ddagger}}{R} - \frac{\Delta H_M}{RT}\right) \quad (11)$$

By adopting this approach, the activation energies associated with the different correlation times can be systematically investigated. In particular, it allows for an accurate determination of the enthalpy associated with inner-sphere water exchange. The activation enthalpy change ($\Delta H_M$) governing the exchange of the coordinated water molecule provides direct insight into both the mechanism and efficiency of the exchange process.[2] Higher $\Delta H_M$ values are indicative of more strongly bound water molecules and, consequently, slower exchange dynamics, whereas lower $\Delta H_M$ values reflect a more labile coordination environment. Because the exchange rate constant $k_{ex}$ depends exponentially on temperature, as described by the Eyring equation, $\Delta H_M$ plays a central role in determining the temperature sensitivity of the exchange process. The determination of this parameter is therefore highly informative, as it allows discrimination among fast-, intermediate-, and slow-exchange regimes, clarifies how ligand architecture and coordination geometry influence metal–water interactions, and ultimately helps to establish whether water exchange is the limiting factor for relaxivity in a given complex. Moreover, Eyring equation (eqn (11)) also allows the determination of the activation entropy change ($\Delta S^{\ddagger}$) associated with the water exchange process. The sign of this parameter can provide insights into the underlying exchange mechanism: dissociative water exchange mechanisms are typically associated with positive $\Delta S^{\ddagger}$ values, whereas associative mechanisms generally exhibit negative $\Delta S^{\ddagger}$ values. It should be emphasized, however, that the sign of $\Delta S^{\ddagger}$ alone does not constitute definitive evidence for the nature of the mechanism.[67,68] A conclusive assignment of the water exchange mechanism would require the determination of acti-

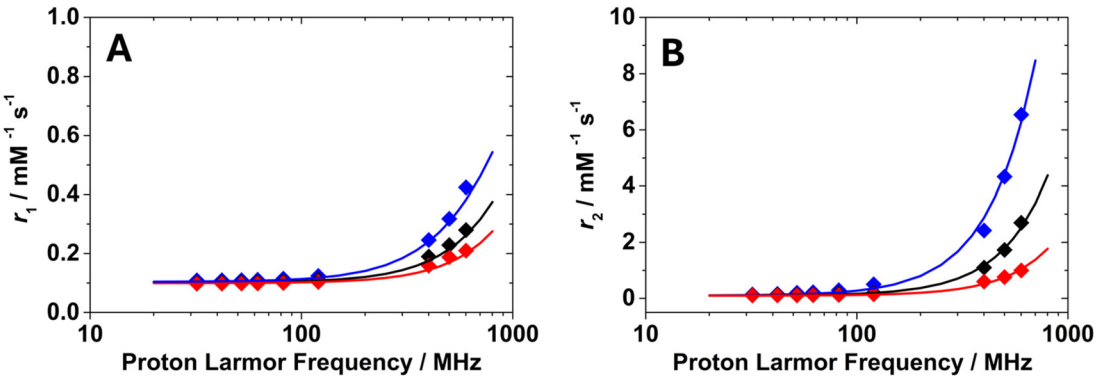


**Fig. 9** $1/T_1$ (A) and $1/T_2$ (B) $^1$H NMRD profiles of $[Dy(DTPA)]^{2-}$ at 283 K (◆), 298 K (◆) and 310 K (◆).

vation volumes, an approach that relies on specialized high-pressure instrumentation that is not readily accessible.[23] The $1/T_1$ and $1/T_2$ $^1$H NMRD profiles collected at 283, 298 and 310 K for $[Dy(DTPA)]^{2-}$ and $[Dy(AAZTA)]^{-}$ are shown in Fig. 9 and S9, respectively.

The experimental profiles were fitted simultaneously, with the resulting best-fit parameters summarized in Table 3. The diffusion coefficient at 298 K ($^{298}D$) and its corresponding activation energy ($E_D$) were fixed to values typical of those reported in the literature. Similarly, the activation energy of the rotational correlation time ($E_R$) was constrained to values characteristic of low molecular weight complexes. Other parameters were fixed to the values obtained from the analysis of the profiles at 298 K, described above. Due to its temperature dependence, the chemical shift difference between the bound and bulk water ($\Delta\omega_M$) was treated as an adjustable parameter, alongside the activation enthalpy ($\Delta H_M$). Excellent fits were achieved; the $\Delta\omega_M$ values across the temperature range were physically reasonable, and the $\Delta H_M$ values yielded activation energies consistent with the distinct water exchange dynamics of the two complexes. Finally, the activation entropy change $\Delta S^{\ddagger}$ was estimated for both complexes, yielding positive values in both cases. These results are consistent with a dissociative mechanism for the exchange of inner-sphere water molecules, generally observed for Ln(III)-based complexes.[2,18,69]

**Table 3** Global analysis of $1/T_1$ and $1/T_2$ NMRD profiles of the $Dy^{3+}$ complexes of DTPA and AAZTA as a function of temperature

| Parameters | $[Dy(DTPA)(H_2O)]^{2-}$ | $[Dy(AAZTA)(H_2O)_2]^{-}$ |
|---|---|---|
| $^{298}\tau_M$ | 27.8 ns[a] | 1.8 μs[a] |
| $\Delta H_M$/kJ mol$^{-1}$ | 13.5 ± 0.5 | 37.5 ± 1.0 |
| $\Delta S^{\ddagger}$/J mol$^{-1}$ K$^{-1}$ | +18[b] | +9[b] |
| $^{298}\tau_R$/ps | 71[a] | 75[a] |
| $E_R$/kJ mol$^{-1}$ | 26.0[a] | 26.0[a] |
| $^{298}\tau_S$/ps | 0.20[a] | 0.22[a] |
| $E_S$/kJ mol$^{-1}$ | 1.0[a] | 1.0[a] |
| $q$ | 1[a] | 2[a] |
| $r$/Å | 3.08[a] | 3.03[a] |
| $a$/Å | 4.0[a] | 4.0[a] |
| $^{298}D/10^5$ cm$^2$ s$^{-1}$ | 2.24[a] | 2.24[a] |
| $E_D$/kJ mol$^{-1}$ | 20.0[a] | 20.0[a] |
| $^{283}\Delta\omega_M/10^5$ rad s$^{-1}$ T$^{-1}$ | 2.03 ± 0.01 | 1.22 ± 0.05 |
| $^{298}\Delta\omega_M/10^5$ rad s$^{-1}$ T$^{-1}$ | 1.49 ± 0.02 | 0.91 ± 0.02 |
| $^{310}\Delta\omega_M/10^5$ rad s$^{-1}$ T$^{-1}$ | 0.99 ± 0.04 | 0.59 ± 0.01 |

[a] Fixed during the fitting. [b] Calculated from the values of $^{298}\tau_M$ and $\Delta H_M$.

## Conclusions

Controlling water exchange dynamics remains one of the most persistent challenges in coordination chemistry. Direct access to the residence time of coordinated water molecules is essential for establishing quantitative structure–property relationships in paramagnetic complexes. Yet, water exchange rates are still predominantly determined by variable-temperature $^{17}$O NMR spectroscopy, a technique that requires high concentrations and therefore excludes scarce, poorly soluble, or supramolecular systems.

Here we overcome these limitations by exploiting the simultaneous analysis of field-dependent $^1$H longitudinal and transverse relaxation rates across the lanthanide series. Moreover, this approach enables the analysis of Ln(III) complexes under significantly more dilute conditions. Although the minimum required concentration depends on the specific system, we estimate that, for prototypical Ln(III) complexes with $q$ = 1 and allowing for reasonable variations in the parameters governing $r_1$, the threshold lies in the range of 1–2 mM for strongly paramagnetic ions (*e.g.*, $Tb^{3+}$, $Dy^{3+}$, $Ho^{3+}$) and 5–10 mM for more weakly paramagnetic ones (*e.g.*, $Pr^{3+}$, $Nd^{3+}$, $Yb^{3+}$). These concentrations are approximately one order of magnitude lower than those typically required for $^{17}$O NMR measurements.[11,12] We show that solvent proton relaxometry provides direct and reliable access not only to exchange kinetics, but also to hydration state, activation parameters, and mechanistic information. This strategy transforms standard relaxometric measurements into a comprehensive probe of solution dynamics.

Application to the $[Ln(DTPA)]^{2-}$ and $[Ln(AAZTA)]^{-}$ families reveals the sensitivity of the method to subtle structural effects. The DTPA series follows a dissociative interchange

mechanism modulated by lanthanide contraction, with progressively faster inner-sphere exchange toward the heavier ions. In striking contrast, the AAZTA analogues display a change in hydration state accompanied by a pronounced deceleration of water exchange for the heavier lanthanides, reaching hundreds of microseconds at the end of the series. The detection of this non-monotonic behaviour provides compelling evidence for steric compression and delicate shifts in hydration equilibria that would be difficult to capture by conventional approaches.

Beyond reproducing known trends, this methodology exposes fine dynamic features that position relaxometry as a quantitative solution-state structural probe, complementary to crystallography and electronic structure calculations. By removing long-standing experimental barriers, it enables routine access to exchange kinetics in systems previously considered inaccessible. This capability opens the door to the predictive design of paramagnetic complexes based on lanthanide or transition metal ions, where the metal–water interface can be engineered with precision to meet targeted functional demands.

## Experimental section

Detailed experimental methods can be found in the SI.

## Author contributions

M. B., F. C., D. L. and C.P.-I. designed the experimental method. M. R., L. R. and D. L. performed the synthesis and characterization of the complexes. M. R. and C.P.-I. carried out the computational analysis. M. B., F. C., M. R., L. R., D. L., C. P.-I. analysed the results. The original draft was written by D. L., M. B. and M. R. and revised by all authors.

## Conflicts of interest

There are no conflicts to declare.

## Data availability

The authors declare that the data supporting the findings of this study are available within the article and its supplementary information (SI). Raw data that support the findings of this study are available from the corresponding author, upon reasonable request. Supplementary information is available. See DOI: **https://doi.org/10.1039/d6qi00419a**.

## Acknowledgements

M. B. acknowledges the project NODES, which has received funding from the Ministero dell'Università e della Ricerca (MUR-M4C2 1.5 of PNRR with grant agreement no. ECS00000036). C. P.-I. thanks Ministerio de Ciencia e Innovación (Grant PID2022-138335NB-I00) and Xunta de Galicia (ED431C 2023/33) for generous financial support and Centro de Supercomputación de Galicia (CESGA) for providing supercomputer facilities.

## References

1 L. Helm and A. E. Merbach, Inorganic and Bioinorganic Solvent Exchange Mechanisms, *Chem. Rev.*, 2005, **105**, 1923–1960.
2 P. Caravan, D. Esteban-Gómez, A. Rodríguez-Rodríguez and C. Platas-Iglesias, Water exchange in lanthanide complexes for MRI applications. Lessons learned over the last 25 years, *Dalton Trans.*, 2019, **48**, 11161–11180.
3 P. Caravan, É. Tóth, A. Rockenbauer and A. E. Merbach, Nuclear and Electronic Relaxation of $Eu^{2+}$(aq) : An Extremely Labile Aqua Ion, *J. Am. Chem. Soc.*, 1999, **121**, 10403–10409.
4 A. Cusanelli, U. Frey, D. T. Richens and A. E. Merbach, The Slowest Water Exchange at a Homoleptic Mononuclear Metal Center: Variable-Temperature and Variable-Pressure $^{17}O$ NMR Study on $[Ir(H_2O)_6]^{3+}$, *J. Am. Chem. Soc.*, 1996, **118**, 5265–5271.
5 J. Wahsner, E. M. Gale, A. Rodríguez-Rodríguez and P. Caravan, Chemistry of MRI Contrast Agents: Current Challenges and New Frontiers, *Chem. Rev.*, 2019, **119**, 957–1057.
6 P. Caravan, C. T. Farrar, L. Frullano and R. Uppal, Influence of molecular parameters and increasing magnetic field strength on relaxivity of gadolinium- and manganese-based $T_1$ contrast agents, *Contrast Media Mol. Imaging*, 2009, **4**, 89–100.
7 S. Zhang, M. Merritt, D. E. Woessner, R. E. Lenkinski and A. D. Sherry, PARACEST Agents: Modulating MRI Contrast via Water Proton Exchange, *Acc. Chem. Res.*, 2003, **36**, 783–790.
8 A. Rodríguez-Rodríguez, M. Zaiss, D. Esteban-Gómez, G. Angelovski and C. Platas-Iglesias, Paramagnetic chemical exchange saturation transfer agents and their perspectives for application in magnetic resonance imaging, *Int. Rev. Phys. Chem.*, 2021, **40**, 51–79.
9 J. A. Peters, The reliability of parameters obtained by fitting of $^1H$ NMRD profiles and $^{17}O$ NMR data of potential $Gd^{3+}$-based MRI contrast agents, *Contrast Media Mol. Imaging*, 2016, **11**, 160–168.
10 S. J. Harley, C. A. Ohlin and W. H. Casey, Geochemical kinetics via the Swift–Connick equations and solution NMR, *Geochim. Cosmochim. Acta*, 2011, **75**, 3711–3725.
11 S. Karimi and L. Helm, Water Exchange on $[Ln(DO3A)(H_2O)_2]$ and $[Ln(DTTA–Me)(H_2O)_2]^-$ Studied by Variable Temperature, Pressure, and Magnetic Field NMR, *Inorg. Chem.*, 2016, **55**, 4555–4563.

12 S. Karimi, L. Tei, M. Botta and L. Helm, Evaluation of Water Exchange Kinetics on $[Ln(AAZTAPh\text{–}NO_2)(H_2O)_q]^x$ Complexes Using Proton Nuclear Magnetic Resonance, *Inorg. Chem.*, 2016, **55**, 6300–6307.

13 B. N. Siriwardena-Mahanama and M. J. Allen, Strategies for Optimizing Water-Exchange Rates of Lanthanide-Based Contrast Agents for Magnetic Resonance Imaging, *Molecules*, 2013, **18**, 9352–9381.

14 S. Aime, M. Chiaussa, G. Digilio, E. Gianolio and E. Terreno, Contrast agents for magnetic resonance angiographic applications: $^1H$ and $^{17}O$ NMR relaxometric investigations on two gadolinium(III) DTPA-like chelates endowed with high binding affinity to human serum albumin, *JBIC, J. Biol. Inorg. Chem.*, 1999, **4**, 766–774.

15 L. Vander Elst, A. Roch, P. Gillis, S. Laurent, F. Botteman, J. W. M. Bulte and R. N. Muller, Dy-DTPA derivatives as relaxation agents for very high field MRI: The beneficial effect of slow water exchange on the transverse relaxivities, *Magn. Reson. Med.*, 2002, **47**, 1121–1130.

16 Z. Baranyai, D. Delli Castelli, C. Platas-Iglesias, D. Esteban-Gomez, A. Bényei, L. Tei and M. Botta, Combined NMR, DFT and X-ray studies highlight structural and hydration changes of $[Ln(AAZTA)]^-$ complexes across the series, *Inorg. Chem. Front.*, 2020, **7**, 795–803.

17 D. Pubanz, G. Gonzalez, D. H. Powell and A. E. Merbach, Unexpectedly Large Change of Water Exchange Rate and Mechanism on $[Ln(DTPA\text{-}BMA)(H_2O)]$ Complexes along the Lanthanide(III) Series, *Inorg. Chem.*, 1995, **34**, 4447–4453.

18 N. Graeppi, D. H. Powell, G. Laurenczy, L. Zékány and A. E. Merbach, Coordination equilibria and water exchange kinetics of lanthanide(III) propylenediaminetetraacetates and other magnetic resonance imaging related complexes, *Inorg. Chim. Acta*, 1995, **235**, 311–326.

19 L. Helm and A. E. Merbach, The Periodic Table and Kinetics?, *CHIMIA*, 2019, **73**, 179–184.

20 S. Zhang, K. Wu, M. C. Biewer and A. D. Sherry, $^1H$ and $^{17}O$ NMR detection of a lanthanide-bound water molecule at ambient temperatures in pure water as solvent, *Inorg. Chem.*, 2001, **40**(17), 4284–4290.

21 D. Cicolari, F. Santanni, L. Grassi, F. Brero, M. Filibian, T. Recca, P. Arosio, M. Perfetti, M. Mariani, R. Sessoli and A. Lascialfari, Longitudinal and transverse NMR relaxivities of Ln(III)-DOTA complexes: A comprehensive investigation, *J. Chem. Phys.*, 2021, **155**, 214201.

22 R. B. Lauffer, Paramagnetic metal complexes as water proton relaxation agents for NMR imaging: theory and design, *Chem. Rev.*, 1987, **87**, 901–927.

23 A. S. Merbach, L. Helm and É. Tóth, *The Chemistry of Contrast Agents in Medical Magnetic Resonance Imaging*, John Wiley & Sons, 2013.

24 A. M. Funk, K.-L. N. A. Finney, P. Harvey, A. M. Kenwright, E. R. Neil, N. J. Rogers, P. K. Senanayake and D. Parker, Critical analysis of the limitations of Bleaney's theory of magnetic anisotropy in paramagnetic lanthanide coordination complexes, *Chem. Sci.*, 2015, **6**, 1655–1662.

25 I. Solomon, Relaxation Processes in a System of Two Spins, *Phys. Rev.*, 1955, **99**, 559–565.

26 I. Solomon and N. Bloembergen, Nuclear Magnetic Interactions in the HF Molecule, *J. Chem. Phys.*, 1956, **25**, 261–266.

27 N. Bloembergen and L. O. Morgan, Proton Relaxation Times in Paramagnetic Solutions. Effects of Electron Spin Relaxation, *J. Chem. Phys.*, 1961, **34**, 842–850.

28 N. Bloembergen, Proton Relaxation Times in Paramagnetic Solutions, *J. Chem. Phys.*, 1957, **27**, 572–573.

29 D. R. Lide, *CRC Handbook of Chemistry and Physics: A Ready-reference Book of Chemical and Physical Data*, CRC Press, 1995.

30 P. Thakur, J. L. Conca, C. J. Dodge, A. J. Francis and G. R. Choppin, Complexation thermodynamics and structural studies of trivalent actinide and lanthanide complexes with DTPA, MS-325 and HMDTPA, *Radiochim. Acta*, 2013, **101**, 221–232.

31 L. Fusaro, F. Mocci, R. N. Muller and M. Luhmer, Insight into the Dynamics of Lanthanide-DTPA Complexes As Revealed by Oxygen-17 NMR, *Inorg. Chem.*, 2012, **51**, 8455–8461.

32 K. Micskei, L. Helm, E. Brucher and A. E. Merbach, Oxygen-17 NMR study of water exchange on gadolinium polyaminopolyacetates $[Gd(DTPA)(H_2O)]^{2-}$ and $[Gd(DOTA)(H_2O)]^-$ related to NMR imaging, *Inorg. Chem.*, 1993, **32**, 3844–3850.

33 G. Tian, L. R. Martin, Z. Zhang and L. Rao, Thermodynamic, Spectroscopic, and Computational Studies of Lanthanide Complexation with Diethylenetriaminepentaacetic Acid: Temperature Effect and Coordination Modes, *Inorg. Chem.*, 2011, **50**, 3087–3096.

34 D. H. Powell, O. M. N. Dhubhghaill, D. Pubanz, L. Helm, Y. S. Lebedev, W. Schlaepfer and A. E. Merbach, Structural and Dynamic Parameters Obtained from $^{17}O$ NMR, EPR, and NMRD Studies of Monomeric and Dimeric $Gd^{3+}$ Complexes of Interest in Magnetic Resonance Imaging: An Integrated and Theoretically Self-Consistent Approach, *J. Am. Chem. Soc.*, 1996, **118**, 9333–9346.

35 J. A. Peters, Multinuclear NMR study of lanthanide(III) complexes of diethylenetriaminepentaacetate, *Inorg. Chem.*, 1988, **27**, 4686–4691.

36 A. Mondry and P. Starynowicz, Optical spectroscopy of neodymium(III) complexes with diethylenetriaminepentaacetic acid in solution and in $[C(NH_2)_3]_2[Nd(dtpa)(H_2O)]P_7H_2O$ single crystal, *Polyhedron*, 2000, **19**, 771–777.

37 Q. Liu, F. Wan, L.-X. Qiu, Y.-Q. Sun and Y.-P. Chen, Four 2D Ln–Cd heterometal–organic coordination polymers based on tetranuclear Ln–Cd oxo-cluster with highly selective luminescent sensing of organic molecules and metal cations, *RSC Adv.*, 2014, **4**, 27013–27021.

38 R. Janicki and A. Mondry, Structural and thermodynamic aspects of hydration of Gd(III) systems, *Dalton Trans.*, 2019, **48**, 3380–3391.

 

39 B. Rodríguez-Barea, J. Mayans, R. Rabelo, A. Sanchis-Perucho, N. Moliner, J. Martínez-Lillo, M. Julve, F. Lloret, R. Ruiz-García and J. Cano, Holmium(III) Single-Ion Magnet for Cryomagnetic Refrigeration Based on an MRI Contrast Agent Derivative, *Inorg. Chem.*, 2021, **60**, 12719–12723.

40 K. I. Hardcastle, M. Botta, M. Fasano and G. Digilio, Experimental Evidence for a Second Coordination Sphere Water Molecule in the Hydration Structure of YbDTPA – Insights for a Re-Assessment of the Relaxivity Data of GdDTPA, *Eur. J. Inorg. Chem.*, 2000, **2000**, 971–977.

41 I. Bertini, C. Luchinat and G. Parigi, *Solution NMR of paramagnetic molecules: applications to metallobiomolecules and models (Vol. 2)*, Elsevier, 2001.

42 I. Bertini, F. Capozzi, C. Luchinat, G. Nicastro and Z. Xia, Water proton relaxation for some lanthanide aqua ions in solution, *J. Phys. Chem.*, 1993, **97**, 6351–6354.

43 S. Aime, M. Botta and G. Ermondi, NMR study of solution structures and dynamics of lanthanide(III) complexes of DOTA, *Inorg. Chem.*, 1992, **31**, 4291–4299.

44 S. Aime, L. Barbero, M. Botta and G. Ermondi, Determination of MetaI-Proton Distances and Electronic Relaxation Times in Lanthanide Complexes by Nuclear Magnetic Resonance Spectroscopy, *Dalton Trans.*, 1992, 225–228.

45 P. D. Burns and G. N. La Mar, Proton spin relaxation for the nonlabile coordinated chelate in lanthanide shift reagents, *J. Magn. Reson.*, 1982, **46**, 61–68.

46 L. Vander Elst, A. Roch, P. Gillis, S. Laurent, F. Botteman, J. W. M. Bulte and R. N. Muller, Dy-DTPA derivatives as relaxation agents for very high field MRI: The beneficial effect of slow water exchange on the transverse relaxivities, *Magn. Reson. Med.*, 2002, **47**, 1121–1130.

47 J.-D. Chai and M. Head-Gordon, Long-range corrected hybrid density functionals with damped atom–atom dispersion corrections, *Phys. Chem. Chem. Phys.*, 2008, **10**, 6615.

48 F. Weigend and R. Ahlrichs, Balanced basis sets of split valence, triple zeta valence and quadruple zeta valence quality for H to Rn: Design and assessment of accuracy, *Phys. Chem. Chem. Phys.*, 2005, **7**, 3297.

49 M. Dolg, H. Stoll, A. Savin and H. Preuss, Energy-adjusted pseudopotentials for the rare earth elements, *Theor. Chim. Acta*, 1989, **75**, 173–194.

50 J. Tomasi, B. Mennucci and R. Cammi, Quantum Mechanical Continuum Solvation Models, *Chem. Rev.*, 2005, **105**, 2999–3094.

51 D. Esteban-Gómez, A. de Blas, T. Rodríguez-Blas, L. Helm and C. Platas-Iglesias, Hyperfine Coupling Constants on Inner-Sphere Water Molecules of Gd(III)-Based MRI Contrast Agents, *ChemPhysChem*, 2012, **13**, 3640–3650.

52 M. Regueiro-Figueroa and C. Platas-Iglesias, Toward the Prediction of Water Exchange Rates in Magnetic Resonance Imaging Contrast Agents: A Density Functional Theory Study, *J. Phys. Chem. A*, 2015, **119**, 6436–6445.

53 J. A. Peters, K. Djanashvili, C. F. Geraldes and C. Platas-Iglesias, The chemical consequences of the gradual decrease of the ionic radius along the Ln-series, *Coord. Chem. Rev.*, 2020, **406**, 213146.

54 A. M. Funk, P. H. Fries, P. Harvey, A. M. Kenwright and D. Parker, Experimental Measurement and Theoretical Assessment of Fast Lanthanide Electronic Relaxation in Solution with Four Series of Isostructural Complexes, *J. Phys. Chem. A*, 2013, **117**, 905–917.

55 C. Harriswangler, F. Lucio-Martínez, L. Godec, L. K. Soro, S. Fernández-Fariña, L. Valencia, A. Rodríguez-Rodríguez, D. Esteban-Gómez, L. J. Charbonnière and C. Platas-Iglesias, Effect of Magnetic Anisotropy on the $^{1}$H NMR Paramagnetic Shifts and Relaxation Rates of Small Dysprosium(III) Complexes, *Inorg. Chem.*, 2023, **62**, 14326–14338.

56 R. Pujales-Paradela, T. Savić, P. Pérez-Lourido, D. Esteban-Gómez, G. Angelovski, M. Botta and C. Platas-Iglesias, Lanthanide Complexes with $^{1}$H paraCEST and $^{19}$F Response for Magnetic Resonance Imaging Applications, *Inorg. Chem.*, 2019, **58**, 7571–7583.

57 R. D. Shannon, Revised effective ionic radii and systematic studies of interatomic distances in halides and chalcogenides, *Acta Crystallogr., Sect. A*, 1976, **32**, 751–767.

58 J. Zhang and M. Dolg, Labile Capping Bonds in Lanthanide(III) Complexes: Shorter and Weaker, *J. Phys. Chem. A*, 2015, **119**, 774–780.

59 A. Rodríguez-Rodríguez, M. Regueiro-Figueroa, D. Esteban-Gómez, T. Rodríguez-Blas, V. Patinec, R. Tripier, G. Tircsó, F. Carniato, M. Botta and C. Platas-Iglesias, Definition of the Labile Capping Bond Effect in Lanthanide Complexes, *Chem. – Eur. J.*, 2017, **23**, 1110–1117.

60 R. M. Badger, The Relation Between the Internuclear Distances and Force Constants of Molecules and Its Application to Polyatomic Molecules, *J. Chem. Phys.*, 1935, **3**, 710–714.

61 S. Aime, G. Bombieri, C. Cavallotti, G. B. Giovenzana, D. Imperio and N. Marchini, An unusual gadolinium ten-coordinated dimeric complex in the series of MRI contrast agents: Na[Gd($H_2O$)AAZTA]·3$H_2O$, *Inorg. Chim. Acta*, 2008, **361**, 1534–1541.

62 S. Aime, L. Calabi, C. Cavallotti, E. Gianolio, G. B. Giovenzana, P. Losi, A. Maiocchi, G. Palmisano and M. Sisti, [Gd-AAZTA]$^{-}$ : A New Structural Entry for an Improved Generation of MRI Contrast Agents, *Inorg. Chem.*, 2004, **43**, 7588–7590.

63 D. Delli Castelli, L. Tei, F. Carniato, S. Aime and M. Botta, [Yb(AAZTA)($H_2O$)]$^{-}$ : an unconventional ParaCEST MRI probe, *Chem. Commun.*, 2018, **54**, 2004–2007.

64 D. Lalli, F. Carniato, L. Tei, C. Platas-Iglesias and M. Botta, Surprising Complexity of the [Gd(AAZTA)($H_2O$)$_2$]$^{-}$ Chelate Revealed by NMR in the Frequency and Time Domains, *Inorg. Chem.*, 2022, **61**, 496–506.

65 D. Lalli, I. Hawala, M. Ricci, F. Carniato, L. D. D'Andrea, L. Tei and M. Botta, Derivatives of GdAAZTA Conjugated to Amino Acids: A Multinuclear and Multifrequency NMR Study, *Inorg. Chem.*, 2022, **61**, 13199–13209.

66 H. Eyring, The Activated Complex in Chemical Reactions, *J. Chem. Phys.*, 1935, **3**, 107–115.

67 F. Peccati and G. Jiménez-Osés, Enthalpy–Entropy Compensation in Biomolecular Recognition: A Computational Perspective, *ACS Omega*, 2021, **6**, 11122–11130.
68 U. Ryde, A fundamental view of enthalpy–entropy compensation, *Med. Chem. Commun.*, 2014, **5**, 1324–1336.
69 C. Platas-Iglesias, D. M. Corsi, L. V. Elst, R. N. Muller, D. Imbert, J.-C. G. Bünzli, É. Tóth, T. Maschmeyer and J. A. Peters, Stability, structure and dynamics of cationic lanthanide(iii) complexes of N,N-bis(propylamide)ethylenediamine-N,N-diacetic acid, *Dalton Trans.*, 2003, 727–737.